TAMPERE UNIVERSITY OF TECHNOLOGY

Multi-Axial Sliced Finite Element Model for Toroidal Inductors

Citation
Panchal, J., Lehikoinen, A., & Rasilo, P. (2019). Multi-Axial Sliced Finite Element Model for Toroidal Inductors. *IEEE Transactions on Magnetics*, *56*(1), [7400106]. https://doi.org/10.1109/TMAG.2019.2950181

Year
2019

Version
Peer reviewed version (post-print)

Link to publication
TUTCRIS Portal (http://www.tut.fi/tutcris)

Published in
IEEE Transactions on Magnetics

DOI
10.1109/TMAG.2019.2950181

Take down policy
If you believe that this document breaches copyright, please contact cris.tau@tuni.fi, and we will remove access to the work immediately and investigate your claim.

Download date:16.04.2021

© 2019 IEEE. Personal use of this material is permitted. Permission from IEEE must be obtained for all other uses, in any current or future media, including reprinting/republishing this material for advertising or promotional purposes, creating new collective works, for resale or redistribution to servers or lists, or reuse of any copyrighted component of this work in other works.

Multi-Axial Sliced Finite Element Model for Toroidal Inductors

Jay Panchal[1], Antti Lehikoinen[2], Paavo Rasilo[1]

[1]Unit of Electrical Engineering, Tampere University, FI-33014 Tampere University, Finland
[2]Department of Electrical Engineering and Automation, Aalto University, FI-00076 Aalto, Finland
jay.panchal@tuni.fi

This paper demonstrates a novel approach for analyzing 3-D electromagnetic fields in toroidal inductors with minimal computational time and resources. A 2-D magnetodynamic finite element (FE) problem is solved in several axial and radial slices of the 3-D inductor geometry using the AVI-formulation. A procedure to couple the slices with each other through circuit equations and suitable interface conditions is proposed. The obtained results are validated with a 3-D FE model in a time-harmonic case. The modelling shows massive reduction in computation time compared to traditional 3-D FE analysis.

Index Terms— **Eddy currents, finite element analysis, inductor, proximity effect, skin effect, winding loss, winding resistance.**

I. INTRODUCTION

THE IMPROVEMENTS in semiconductors and soft-switching topologies have made higher switching frequency operations possible for power converters. Such high frequency operations drastically influence the design of magnetic components in power electronics. Especially, the presence of skin and proximity effects in the windings of magnetic components cannot be neglected at high switching frequencies.

The skin effect is a result of eddy currents flowing under the influence of the local magnetic field of a conductor, while proximity effect refers to eddy currents induced by an external magnetic field. In particular, under presence of such frequency dependent effects, windings of power magnetic components share the highest percentage of loss at high frequencies [1]-[3]. For getting most optimal designs, skin and proximity effects need thorough treatment during modelling stage.

At high frequencies, eddy current effects in windings with multiple strands (sub-conductors) become too complex for conventional analytical methods [4], [5]. Parameters like porosity factor and changing penetration depth require tuning of analytical methods based on experiments or heavy numerical simulations [6].

Several loss models have been developed to reduce the computation times and to reach accuracy levels as high as possible [7]-[10]. However, precise analytical models of the fields in problems like windings with multiple stranded conductors or any asymmetrical winding structures are missing [11]. This makes it difficult for industry to completely rely on analytical or empirical methods for design of magnetic components. Hence, numerical methods based on two dimensional (2-D) and three dimensional (3-D) approaches are the preferred alternatives for better reliability and accuracy. Although 2-D finite element (FE) method (FEM) is an ideal choice considering computational time and cost, the traditional 2-D FEM stays limited to simple structures. Therefore, to attain high level of precision, the 3-D FEM has to be used for optimization.

3-D FE analysis of eddy currents and circulating currents in the inductors and transformers with multiple parallel conductors would require fine 3-D discretization of each wire. The entire problem becomes substantially big for solving in a single computer system. For addressing these issues, there have been concrete efforts in [12] and [13] for analyzing complex winding structures. An approach combining rotationally symmetric 2-D and 3-D simulation was presented in [12]. The method presented in [13] is based on the partial element equivalent circuit (PEEC). For the precise computations in case of inductors with ferromagnetic cores, PEEC has been combined with the boundary element method in [14] and with FEM in [15]. The method is consistently being developed for accurate modelling of linear inhomogeneous conductive and magnetic media [16]-[19]. PEEC is also extended for different loss models for coreless inductors [20]. However, for exploring inhomogeneous distribution of current density in winding conductors at high frequency, FEM is still seen as more robust and reliable approach [5], [21].

This paper presents a computationally efficient and optimal method for exploring 3-D eddy current effects in the winding of toroidal inductors used in power conversion units. The idea is based on coupled solution of electromagnetic fields in 2-D slices taken axially and radially from the inductor. The approach will be called a multi-axial slice model (MASM).

As a test case, a single symmetry sector of a toroidal inductor with an equally distributed winding is considered. Since the paper targets on providing the concept of MASM, two simplified windings with one and three parallel sub-conductors are considered. The MASM is created in the MATLAB environment. For validating the proposed modelling approach, comparison is made against 3-D simulations from COMSOL Multiphysics. Section II covers the theoretical aspects about the MASM. It also includes details about the geometry and supporting technical aspects for the simulations. Along with the necessary results, Section III provides in-depth comparative analysis followed by conclusions in Section IV. We widely use the definitions explained in [22], [23].

II. MODELLING METHODOLOGY

A. Geometric model

Fig. 1 shows the considered toroidal inductor as well as one of its symmetry sectors. Both the MASM and 3-D FEM are built for the symmetry sector. A linear ferrite core with relative

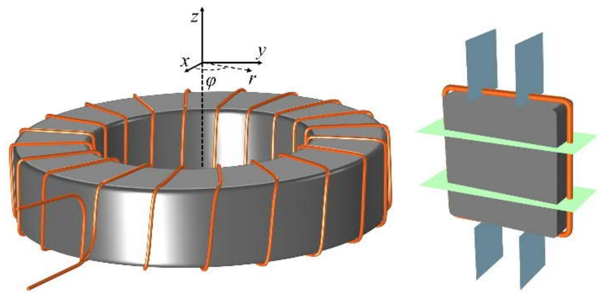

Fig. 1. Approximation of one symmetry sector of a toroidal inductor by two axial (in green) and two radial (in blue) slices.

permeability μ_r= 3000 is considered. The inner and outer radiuses of the core are designated by r_m and r_out, respectively.

The height of the core is h. A copper conductor with 0.6 mm diameter is used. The inductor carries N = 50 turns equally distributed over the periphery as shown in Fig.1. The symmetry sector covers an angle of $\varphi_\mathrm{sym} = 2\pi / N$.

In Fig. 1, the symmetry sector is sliced with four planes, two axial ones in green (z = constant) and two radial ones in blue (r = constant), so that the current-carrying conductors are approximately perpendicular to each slice. The axial slices allow accounting for the magnetic core as well as the conductors at the inner and outer sides of the core. The radial slices allow accounting for the stray field on the top and bottom of the core. The core is only considered in the axial slices, not in the radial ones.

In general, we can consider n_axi axial slices and n_rad radial slices, indexing the slices with $k = 1, \ldots, n_\mathrm{axi} + n_\mathrm{rad}$. We assume that the winding consists of n_par parallel conductors, which means that each 2-D slice will include $2n_\mathrm{par}$ distinct conductor regions corresponding to the positive and negative coils sides. The conductor regions Ω_{kq} are indexed with $q = 1, \ldots, 2n_\mathrm{par}$ and the parallel paths with $p = 1, \ldots, n_\mathrm{par}$.

B. *Equations in one slice*

The magnetic field in each slice k is mostly parallel to the slice plane, and can be analyzed comfortably using 2-D FE analysis. In this paper, the AVI formulation [24] is used for the field analysis. The governing equations for the 2-D electromagnetic field in slice k associated with a perpendicular length l_k are given by

$$-\nabla \cdot \nu \nabla A_k = 0 \tag{1}$$

outside the conductors, and

$$-\nabla \cdot \nu \nabla A_k + \sigma \frac{\partial A_k}{\partial t} - \sigma \frac{u_{kq}}{l_k} = 0 \tag{2}$$

in Ω_{kq}. In the equations, A_k is the component of the magnetic vector potential perpendicular to the slice, u_{kq} is the potential difference in Ω_{kq}, ν is the reluctivity and σ is the electrical conductivity. The current in the conductor branch p is given by

$$i_p = -m_{kqp} \int_{\Omega_{ki}} \sigma \frac{\partial A_k}{\partial t} d\Omega_{kq} + m_{kqp} \frac{u_{kq}}{R_{kq}} \quad \text{for each } k \tag{3}$$

where m_{kqp} associates the currents p with regions Ω_{kq} according to

$$m_{kqp} = \begin{cases} +1, \text{ if current of branch } p \text{ flows in the positive} \\ \quad \text{direction through } \Omega_{kq} \\ -1, \text{ if current of branch } p \text{ flows in the negative} \\ \quad \text{direction through } \Omega_{kq} \\ 0, \text{ otherwise} \end{cases}$$

and R_{kq} is the resistance of corresponding to domain Ω_{kq}. It is emphasized that the currents are common for each slice, so that i_p is independent of k. Now based on (3), the voltage over conductor domains Ω_{kq} is expressed as

$$u_{kq} = m_{kqp} R_{kq} i_p + R_{kq} \int_{\Omega_{kq}} \sigma \frac{\partial A_k}{\partial t} d\Omega_{kq} \tag{4}$$

The voltage over each conductor p in each slice k is

$$U_{kp} = \sum_q m_{kqp} u_{kq} \tag{5}$$

Discretizing (2) and (4) with the Galerkin method yields

$$\begin{bmatrix} \boldsymbol{S}_k + \boldsymbol{T}_k \dfrac{d}{dt} & \boldsymbol{D}_{\Omega,k} & \boldsymbol{0} \\ \boldsymbol{C}_{\Omega,k} \dfrac{d}{dt} & -\boldsymbol{I} & \boldsymbol{R}_k \boldsymbol{M}_k \\ \boldsymbol{0} & \boldsymbol{M}_k^\mathrm{T} & \boldsymbol{0} \end{bmatrix} \begin{bmatrix} \boldsymbol{a}_k \\ \boldsymbol{u}_k \\ \boldsymbol{i} \end{bmatrix} = \begin{bmatrix} \boldsymbol{0} \\ \boldsymbol{0} \\ \boldsymbol{U}_k \end{bmatrix} \tag{6}$$

where $\boldsymbol{a}_k$ contains the nodal values of A_k, $\boldsymbol{u}_k$ contains u_{kq} and $\boldsymbol{i}$ contains i_p. $\boldsymbol{S}_k$ and $\boldsymbol{T}_k$ are the stiffness and damping matrices respectively. $\boldsymbol{D}_{\Omega,k}$ and $\boldsymbol{C}_{\Omega,k}$ are related to the field source and the back-emf induced to the conductors, respectively. They are obtained as

$$\left[\boldsymbol{D}_{\Omega,k}\right]_{nq} = -\frac{\sigma}{l_k} \int_{\Omega_{kq}} w_n d\Omega_{kq} \tag{7}$$

$$\left[\boldsymbol{C}_{\Omega,k}\right]_{qn} = \sigma R_{kq} \int_{\Omega_{kq}} w_n d\Omega_{kq} \tag{8}$$

where w_n is the FE shape function associated with node n. $\boldsymbol{M}_k$ represents the coupling matrix for conductor domains and parallel branches according to (5), and $\boldsymbol{R}_k$ is the diagonal matrix for conductor resistances R_{kq}:

$$\left[\boldsymbol{M}_k\right]_{qp} = m_{kqp} \tag{9}$$

$$\left[\boldsymbol{R}_k\right]_{qq} = R_{kq} \tag{10}$$

C. *Multi-axial slice model and simulation*

As shown in Fig.2, the toroidal inductor is assumed to be placed in the cylindrical coordinate system r-φ-z so that the core covers the region $[-h/2\ h/2] \times [r_\mathrm{in}\ r_\mathrm{out}] \times [-\varphi_\mathrm{sym}/2\ \varphi_\mathrm{sym}/2]$. The axial slices are equally-sized circular sectors $[0\ r_\mathrm{max}] \times [-\varphi_\mathrm{sym}/2\ \varphi_\mathrm{sym}/2]$ chosen from axial positions z_k corresponding to n_axi-point Gauss quadrature points over $z \in [-h/2\ h/2]$. The relative perpendicular lengths l_k / h correspond to Gauss integration weights. The fields in the axial slices are described in x-y

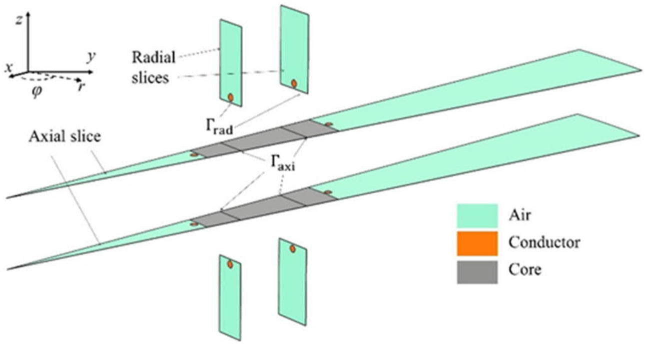

Fig. 2. Axial and radial slice models with interface conditions.

coordinates, so that A_k corresponds to the z-component of the vector potential.

The radial slices consist of two separate planes $[h/2\ h_{\mathrm{max}}/2] \times [-\varphi_{\mathrm{sym}}/2\ \varphi_{\mathrm{sym}}/2]$ and $[-h_{\mathrm{max}}/2\ -h/2] \times [-\varphi_{\mathrm{sym}}/2\ \varphi_{\mathrm{sym}}/2]$ on the top and bottom of the core chosen from radial positions r_k corresponding to n_{rad}-point Gauss quadrature points over $r \in [r_{\mathrm{in}}\ r_{\mathrm{out}}]$. The relative perpendicular lengths $l_k\ /\ (r_{\mathrm{out}}\ -\ r_{\mathrm{in}})$ correspond to Gauss integration weights. The fields in the radial slices are described in $r_k\varphi$-z coordinates, where r_k is constant in each slice. Thus, the width of the slices increases as we move radially outwards (Fig.2). By change of variables, $r_k\varphi \rightarrow x$, $z \rightarrow y$ and $r \rightarrow z$, the fields can be handled similarly to the axial slices.

The FE systems of each slice can be written as a large uncoupled system

$$\begin{bmatrix} \boldsymbol{S}+\boldsymbol{T}\dfrac{d}{dt} & \boldsymbol{D}_{\Omega} & \boldsymbol{0} \\ \boldsymbol{C}_{\Omega}\dfrac{d}{dt} & -\boldsymbol{I} & \boldsymbol{RM} \\ \boldsymbol{0} & \boldsymbol{M}^{\mathrm{T}} & \boldsymbol{0} \end{bmatrix} \begin{bmatrix} \boldsymbol{a} \\ \boldsymbol{u} \\ \boldsymbol{i} \end{bmatrix} = \begin{bmatrix} \boldsymbol{0} \\ \boldsymbol{0} \\ \boldsymbol{U} \end{bmatrix}, \tag{11}$$

where matrices $\boldsymbol{S}$, $\boldsymbol{T}$, $\boldsymbol{D}_{\Omega}$ and $\boldsymbol{C}_{\Omega}$ are block diagonal matrices assembled from $\boldsymbol{S}_k$, $\boldsymbol{T}_k$, $\boldsymbol{D}_{\Omega,k}$ and $\boldsymbol{C}_{\Omega,k}$, $\boldsymbol{a}$ and $\boldsymbol{u}$ are vectors containing $\boldsymbol{a}_k$ and $\boldsymbol{u}_k$, and

$$\boldsymbol{R} = \sum_k \boldsymbol{R}_k\ ,\ \boldsymbol{M} = \sum_k \boldsymbol{M}_k \text{ and } \boldsymbol{U} = \sum_k \boldsymbol{U}_k \tag{12}$$

are summed over the slices. $\boldsymbol{R}$ and $\boldsymbol{U}$ contain the total resistances and total voltages affecting over each conductor p in one symmetry sector.

The idea of the MASM comes into picture after coupling axial and radial slices. The coupling includes three conditions:

1. Forcing the total currents in each conductor to be equal in each slice.
2. Forcing the tangential magnetic fields $\boldsymbol{H}\cdot\boldsymbol{u}_{\varphi}$ at the interfaces between the radial and axial slices to be continuous in the weak sense.
3. Accounting for the perpendicular flux crossing the interfaces between the radial and axial slices.

Condition 1 is satisfied automatically in the AVI formulation, since the currents are common for each slice. Condition 2 is implemented through a non-homogeneous Neumann condition in the radial slices k as

$$\int_{\Gamma_{\mathrm{rad},k}} w_n \boldsymbol{H}\cdot\boldsymbol{u}_{\varphi} d\Gamma = \int_{\Gamma_{\mathrm{axi},k}} w_n \boldsymbol{H}\cdot\boldsymbol{u}_{\varphi} d\Gamma \tag{13}$$

where $\Gamma_{\mathrm{rad},k}$ is the boundary of radial slice $k = n_{\mathrm{axi}} + 1, \ldots, n_{\mathrm{axi}} + n_{\mathrm{rad}}$ at the top ($z = h/2$) or bottom ($z = -h/2$) surface of the core, and $\Gamma_{\mathrm{axi},k}$ is the corresponding boundary in the top or bottom axial slice. However, to avoid complex interpolations between two possibly non-conforming meshes, we derive here a simple approach by approximating the circumferential field strength in radial slice k as

$$\boldsymbol{H}\cdot\boldsymbol{u}_{\varphi} = \frac{NI}{2\pi r_k} \tag{14}$$

where

$$I = \sum_{p=1}^{n_{\mathrm{par}}} i_p \tag{15}$$

is the total current carried by the n_{par} parallel conductors in one symmetry sector. When (14) and (15) are substituted in right-hand-side of (13), a non-homogeneous Neumann condition for the radial slices is obtained. The FE block matrix thus becomes

$$\begin{bmatrix} \boldsymbol{S}+\boldsymbol{T}\dfrac{d}{dt} & \boldsymbol{D}_{\Omega} & \boldsymbol{D}_{\Gamma} \\ \boldsymbol{C}_{\Omega}\dfrac{d}{dt} & -\boldsymbol{I} & \boldsymbol{RM} \\ \boldsymbol{0} & \boldsymbol{M}^{\mathrm{T}} & \boldsymbol{0} \end{bmatrix} \begin{bmatrix} \boldsymbol{a} \\ \boldsymbol{u} \\ \boldsymbol{i} \end{bmatrix} = \begin{bmatrix} \boldsymbol{0} \\ \boldsymbol{0} \\ \boldsymbol{U} \end{bmatrix} \tag{16}$$

where the additional matrix $\boldsymbol{D}_{\Gamma}$ is a vertical assembly of matrices

$$\left[\boldsymbol{D}_{\Gamma,k}\right]_{np} = \frac{N}{2\pi r_k} \int_{\Gamma_{\mathrm{rad},k}} w_n d\Gamma \tag{17}$$

for all p and for $k = n_{\mathrm{axi}} + 1, \ldots, n_{\mathrm{axi}} + n_{\mathrm{rad}}$, which account for the tangential field strength in the radial slices.

Condition 3 could perhaps be implemented by considering the flux crossing the interface as a non-zero divergence of the flux-density in the axial slices. However, this would be challenging to implement. We thus again derive a simpler approach using the Poynting theorem [25], based on which the power passing through the interface between the radial and axial slices is given by

$$P = \int_{r_{\mathrm{in}}}^{r_{\mathrm{out}}} \int_{-\varphi_{\mathrm{sym}}/2}^{\varphi_{\mathrm{sym}}/2} r\boldsymbol{E}\times\boldsymbol{H}\cdot\boldsymbol{u}_z d\varphi dr \tag{18}$$

where $\boldsymbol{E}$ is the electric field strength. Since the radial slices are placed at the Gauss quadrature points, we can write the integral as

$$P = \sum_{k=n_{\mathrm{axi}}+1}^{n_{\mathrm{axi}}+n_{\mathrm{rad}}} l_k \int_{\Gamma_{\mathrm{rad},k}} \boldsymbol{E}\times\boldsymbol{H}\cdot\boldsymbol{u}_z d\Gamma \tag{19}$$

Using (10) and

$$\boldsymbol{E} = -\frac{\partial A_k}{\partial t}\boldsymbol{u}_{\mathrm{r}} \tag{20}$$

we get

$$P = -NI \sum_{k=n_{\mathrm{axi}}+1}^{n_{\mathrm{axi}}+n_{\mathrm{rad}}} \frac{l_k}{2\pi r_k} \int_{\Gamma_{\mathrm{rad},k}} \frac{\partial A_k}{\partial t} d\Gamma \tag{21}$$

This power should be seen as a change Δu_p in the conductor potential differences, such that

$$P = NI\Delta u_p \tag{22}$$

meaning that

$$\Delta u_p = -\sum_{k=n_{\mathrm{axi}}+1}^{n_{\mathrm{axi}}+n_{\mathrm{rad}}} \frac{l_k}{2\pi r_k} \int_{\Gamma_{\mathrm{rad},k}} \frac{\partial A_k}{\partial t} d\Gamma \tag{23}$$

for all *p*. This voltage is added to the voltage equation in (5), yielding a final system of

$$\begin{bmatrix} \boldsymbol{S} + \boldsymbol{T}\frac{d}{dt} & \boldsymbol{D}_{\Omega} & \boldsymbol{D}_{\Gamma} \\ \boldsymbol{C}_{\Omega}\frac{d}{dt} & -\boldsymbol{I} & \boldsymbol{RM} \\ \boldsymbol{C}_{\Gamma}\frac{d}{dt} & \boldsymbol{M}^{\mathrm{T}} & \boldsymbol{0} \end{bmatrix} \begin{bmatrix} \boldsymbol{a} \\ \boldsymbol{u} \\ \boldsymbol{i} \end{bmatrix} = \begin{bmatrix} \boldsymbol{0} \\ \boldsymbol{0} \\ \boldsymbol{U} \end{bmatrix} \tag{24}$$

where the additional matrix $\boldsymbol{C}_{\Gamma}$ is a horizontal assembly of matrices

$$\left[\boldsymbol{C}_{\Gamma,k}\right]_{pn} = \frac{-l_k}{2\pi r_k} \int_{\Gamma_{\mathrm{rad},k}} w_n d\Gamma \tag{25}$$

for all p and for $k = n_{\mathrm{axi}} + 1, \ldots, n_{\mathrm{axi}} + n_{\mathrm{rad}}$, which account for the power coming from the radial slices. Note that

$$\boldsymbol{C}_{\Gamma,k} = \frac{-l_k}{N} \boldsymbol{D}_{\Gamma,k}^{\mathrm{T}} . \tag{26}$$

Equation (24) represents the whole MASM system, where the slices are coupled together.

D. 3-D simulation

Time-harmonic 3-D FE simulation with COMSOL Multiphysics is used to validate the proposed MASM. Two test cases with $n_{\mathrm{par}} = 1$ and $n_{\mathrm{par}} = 3$ parallel conductors are simulated. The respective models are represented in Fig.3. The multiple sub-conductor case provides better insight about frequency dependent power losses in each conductors. The chosen geometries are symmetric with respect to the $z = 0$ plane, and thus only the lower half $z \leq 0$ is considered in the 3-D model for minimizing the required computation time and resources. Both halves are considered in the MASM.

A boundary layer mesh is used in the conductor section for accurately capturing the influence of skin effect on power losses. Periodic boundary conditions are used on the sides of the symmetry sector. This ensures the continuity of flux density along the circumferential path of toroid. A voltage is imposed between the inner and outer conductor cross sections in the $z = 0$ plane. The currents and power losses are computed in each conductor for both cases and compared to those obtained from the MASM.

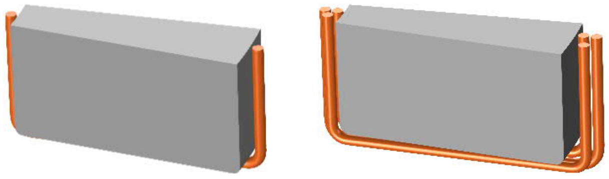

(a) (b)

Fig. 3. 3-D geometric model for (a) winding with single conductor and (b) winding with triple sub-conductor.

III. RESULTS

The simulation results presented here are computed on a single Windows machine with 32 GB RAM and Intel Core i7-8650U (4 cores 8 threads) 1.9 GHz processor. All simulations including 3-D FEM are with linear discretization. The currents and power losses of the MASM and the 3-D FEM for the single-conductor case are shown in Fig. 4. The values are computed over a frequency range from 10 kHz to 1 MHz for sinusoidal voltage input. The current is kept constant by maintaining constant voltage to frequency ratio for all frequencies. This allows good insight on the change in losses as a function of frequency. Each graph shows data for three simulations: the reference results from 3-D FEM, results from the MASM with two axial and two radial slices, as well as results from the MASM with two axial slices, but no radial slices. The last case is done for studying the significance of including the radial slices into the model. In all simulations, the losses increase significantly above 60 kHz. As the frequency increases, the MASM without radial slices underestimates the losses. Thus, simple 2-D FEM fails to capture high frequency 3-D effects in the windings. On the other hand, the results from the MASM with both axial and radial slices agree well with those from the 3-D FEM.

Fig. 5 compares the current density distributions in the axial slices of the MASM to those obtained from the 3-D model in identical locations at 100 kHz. Similar comparison for the current densities in the radial slices is shown in Fig. 6. In this case, distribution of the current density is similar in all slices. The reason is that the conductor is perfectly aligned in the radial and the axial directions. Moreover, in a single conductor case, the skin effect plays the most influential role in the current distribution.

Similar results are produced for the winding with triple sub-conductors. The computed results for the total current and losses are shown in Fig 7. The results from the MASM are very close to the 3-D FEM computations. Again, neglecting the radial slices fails to provide precise information on frequency dependent power loss.

Along with skin effect losses, the triple conductor case also include loss components from proximity effect and circulating currents [26], [27]. The resultant distribution of the current density is shown in Figs. 8 and 9. The former depicts current

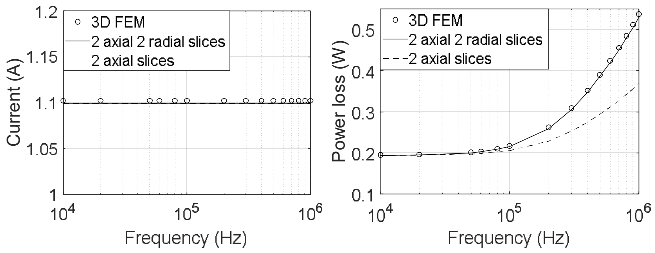

(a) (b)

Fig. 4. Comparison of total (a) current and (b) power loss for the single conductor case.

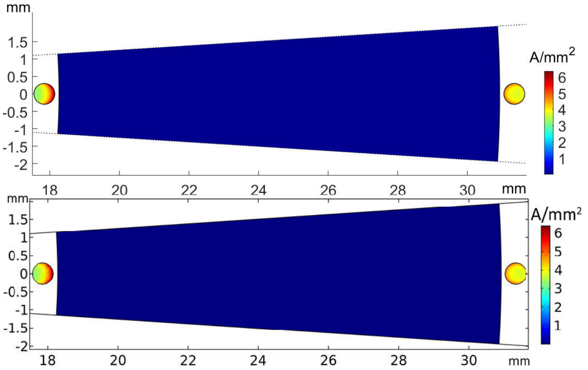

Fig. 5. Current density distribution in the single conductor case: (top) Axial slice of the proposed model, and (bottom) an identical section of the 3-D model.

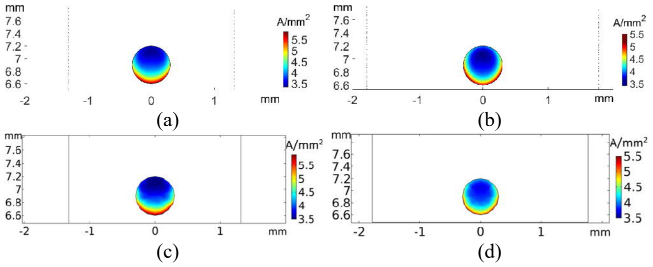

(a) (b) (c) (d)

Fig. 6. Current density distribution in the single conductor case: (a) Inner and (b) outer radial slices of the proposed model, and (c,d) identical sections of the 3-D model.

density in axial direction while the latter shows radially directed current densities. The share of current among the parallel conductors changes as a function of the frequency. The computed currents and losses for each sub-conductor are shown in Fig. 10. The red curves indicate conductor 1, located closest to the core. The conductor 2 and 3 quantities are represented by blue and green curves respectively. As conductor 2 lies right above conductor 1, it has the largest distance from the surface of the core among the conductors. It shares the smallest amount of current at higher frequency, which explains lower AC losses than in the other two conductors. Conductor 3 is located at the intermediate distance between conductors 1 and 2 from the surface of core. For the entire frequency range, the current and power losses of conductor 3 stay between the respective values of conductors 1 and 2.

By having a closer view at the results from simulation with only 2 axial slices, but no radial ones, the computed current values deviate from the 3-D FEM quantities. For the frequency range from 10 kHz to 500 kHz, the currents have higher deviation. At lower and higher frequencies, the currents match well with the 3-D FEM. However, the scenarios are different

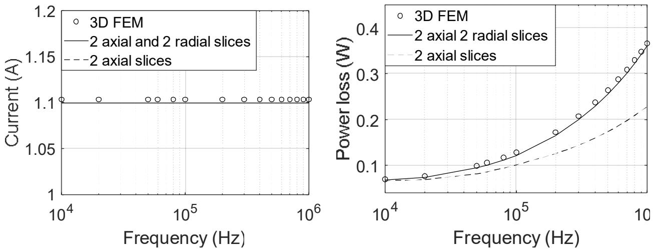

(a) (b)

Fig. 7. Comparison of total (a) current and (b) power loss for the triple conductor case.

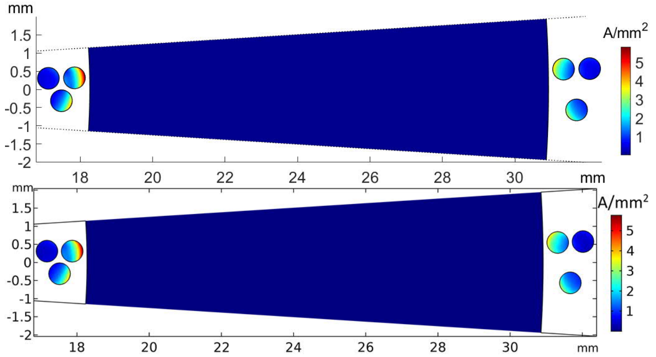

Fig. 8. Current density distribution in the triple conductor case: (top) Axial slice of the proposed model, and (bottom) an identical section of the 3-D model.

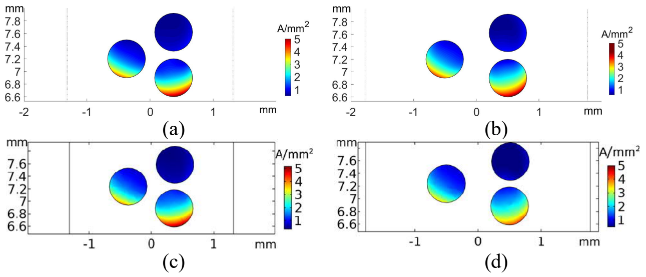

(a) (b) (c) (d)

Fig. 9. Current density distribution in the triple conductor case: (a) Inner and (b) outer radial slices of the proposed model, and (c,d) identical sections of the 3-D model.

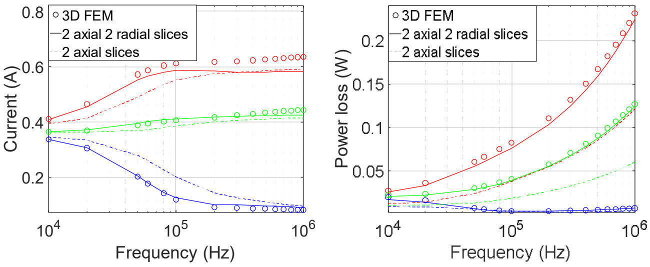

(a) (b)

Fig. 10. Comparison of (a) currents and (b) power losses in each conductor in the triple conductor case.

with power losses. The computed values of losses with the MASM are quite close to the ones from 3-D FEM. The accurate understanding of such quantities is important for deciding the optimal number of parallel conductors in windings [28]. In the same context, simple 2-D FEM with only axial slices does not provide the required accuracy level at high frequencies.

The simulation times for all frequencies were observed in each simulated case. On average, one MASM simulation took 4.91 seconds while one 3-D FEM simulation took 73.4 seconds in the single conductor case. In the triple conductor case, the

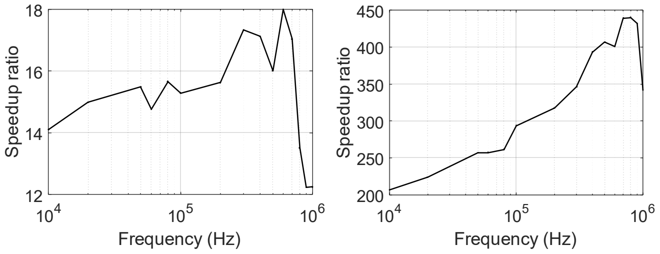

(a) (b)

Fig. 11. Speedup ratio for (a) single conductor and (b) triple conductor case.

MASM took 4.95 seconds while the 3-D FEM took 1325 seconds. The speedup ratio of 3-D FEM and MASM computations are shown in Fig. 11. It is clearly seen that in the single conductor case, the MASM is about 15 times faster compared to 3D FEM. A more significant difference is seen in the triple conductor case, where the MASM is 265.7 times faster on an average scale compared to 3-D FEM analysis. In comparison to 3-D FEM, the computed power losses with MASM are on average less by 2.8% and 3.5% for single and triple conductor cases, respectively.

IV. CONCLUSION

The method proposed here carries potential to replace the usage of 3-D FEM approach for the toroidal inductor modelling. With a reasonable trade-off between accuracy level and simulation time, the proposed multiaxial slice model is promisingly fast. The frequency dependent power losses for multiple conductor winding can easily be analyzed without stressing available computational resources. The obtained results have shown good agreement with the results from 3-D FEM simulation of commercial software.

Based on the results, the implementation of this idea can give an extra edge to industries in cutting down massive amount of time in their design process. As a part of future work, twisting effect of multiple conductor winding for toroidal inductors will be incorporated in the developed method.

ACKNOWLEDGMENT

The foundation of Emil Aaltonen and the Academy of Finland are acknowledged for financial support.

REFERENCES

[1] J. Smajic, J. Hughes, T. Steinmetz, D. Pusch, W. Monig and M. Carlen, "Numerical Computation of Ohmic and Eddy-Current Winding Losses of Converter Transformers Including Higher Harmonics of Load Current," *IEEE Trans. Magn.*, vol. 48, no. 2, pp. 827-830, Feb. 2012.

[2] D. Fu, *Topology Investigation and System Optimization of Resonant Converters*, Ph.D. dissertation, Virginia Polytechnic Institute and State University, Virginia, USA, 2010.

[3] A. Van den Bossche and V. C. Valchev, *Inductors and Transformers for Power Electronics*, CRC Press, Taylor Francis Group, 2005.

[4] G. S. Dimitrakakis and E. C. Tatakis, "High-Frequency Copper Losses in Magnetic Components With Layered Windings," *IEEE Trans. Magn.*, vol. 45, no. 8, pp. 3187-3199, Aug. 2009.

[5] L. Taylor, X. Margueron, Y. Le Menach and P. Le Moigne, "Numerical modelling of PCB planar inductors: impact of 3D modelling on high-frequency copper loss evaluation," *IET Power Electron.*, vol. 10, no. 14, pp. 1966-1974, Nov. 2017.

[6] A. Pereira, F. Sixdenier, M. A. Raulet, B. Lefebvre and N. Burais, "Comparison Between Numerical and Analytical Methods of AC Resistance Evaluation for Medium-Frequency Transformers: Validation on a Prototype and Thermal Impact Analysis," *Can. J. Elect. Comput. Eng.*, vol. 40, no. 2, pp. 101-109, Spring 2017.

[7] E. Langlois, T. Monson, D. Huber and J. Watt, "Finite element modeling of nanoscale-enabled microinductors for power electronics," *J. Mater. Res.*, vol. 33, no. 15, pp. 2223-2233. Aug. 2018.

[8] M. Kaymak, Z. Shen and R. W. De Doncker, "Comparison of analytical methods for calculating the AC resistance and leakage inductance of medium-frequency transformers," *Proc. COMPEL*, Trondheim, pp. 1-8, June 2016.

[9] A. Reatti and M. K. Kazimierczuk, "Comparison of various methods for calculating the AC resistance of inductors," *IEEE Trans. Magn.*, vol. 38, no. 3, pp. 1512-1518, May 2002.

[10] C. R. Sullivan and L. Losses, "Analytical model for effects of twisting on litz-wire losses," *Proc. COMPEL*, Santander, pp. 1-10, June 2014.

[11] E. Plumed, J. Acero, I. Lope and C. Carretero, "3D Finite Element Simulation of Litz Wires with Multilevel Bundle Structure," *Proc. IECON*, Washington, DC, pp. 3479-3484, Oct. 2018.

[12] A. Roßkopf, E. Bär and C. Joffe, "Influence of Inner Skin- and Proximity Effects on Conduction in Litz Wires," *IEEE Trans. Power Electron.*, vol. 29, no. 10, pp. 5454-5461, Oct. 2014.

[13] T. Guillod, J. Huber, F. Krismer and J. W. Kolar, "Litz-wire losses: Effects of twisting imperfections," *Proc. COMPEL*, Stanford, CA, pp. 1-8, July 2017.

[14] I. F. Kovacevic, A. M. Musing and J. W. Kolar, "An Extension of PEEC Method for Magnetic Materials Modeling in Frequency Domain," *IEEE Trans. Magn.*, vol. 47, no. 5, pp. 910-913, May 2011.

[15] A. Roßkopf, E. Bär, C. Joffe and C. Bonse, "Calculation of Power Losses in Litz Wire Systems by Coupling FEM and PEEC Method," *IEEE Trans. Power Electron.*, vol. 31, no. 9, pp. 6442-6449, Sept. 2016.

[16] Y. Hackl, P. Scholz, W. Ackermann and T. Weiland, "Efficient Simulation of Magnetic Components Using the MagPEEC-Method," *IEEE Trans. Magn.*, vol. 53, no. 3, pp. 1-9, Mar. 2017.

[17] R. Torchio, P. Alotto, P. Bettini, D. Voltolina and F. Moro, "A 3-D PEEC Formulation Based on the Cell Method for Full-Wave Analyses With Conductive, Dielectric, and Magnetic Media," *IEEE Trans. Magn.*, vol. 54, no. 3, pp. 1-4, Mar. 2018.

[18] L. Lombardi, D. Romano and G. Antonini, "Analytical Formula for the Magnetic-to-Electric Field Coupling of Magnetization in the Partial Element Equivalent Circuit Method," *IEEE Trans. Magn.*, vol. 54, no. 10, pp. 1-12, Oct. 2018.

[19] R. Torchio, F. Moro, G. Meunier, J. -. Guichon and O. Chadebec, "An Extension of Unstructured-PEEC Method to Magnetic Media," *IEEE Trans. Magn.*, vol. 55, no. 6, pp. 1-4, June 2019.

[20] Z. De Grève, J. Siau, G. Meunier, J. Guichon and O. Chadebec, "A Mixed Surface Volume Integral Formulation for the Modeling of High-Frequency Coreless Inductors," *IEEE Trans. Magn.*, vol. 52, no. 3, pp. 1-4, Mar. 2016.

[21] S. Wang, D. Yuan, A. Wang, K. Liu, H. Li and S. Wang, "Circuit-Field Coupling and Magnetic-Thermal Coupling Analysis of RRF Converter Designed With Magnetic Integration," *IEEE Trans. Magn.*, vol. 55, no. 5, pp. 1-8, May 2019.

[22] A. Lehikoinen, *Circulating and eddy current losses in random-wound electrical machines*, Ph.D. dissertation, Aalto University, Espoo, Finland, 2017.

[23] M. J. Islam, J. Pippuri, J. Perho and A. Arkkio, "Time-harmonic finite-element analysis of eddy currents in the form-wound stator winding of a cage induction motor," *IET Electr. Power App.*, vol. 1, no. 5, pp. 839-846, Sept. 2007.

[24] I. A. Tsukerman, A. Konrad and J. D. Lavers, "A method for circuit connections in time-dependent eddy current problems," *IEEE Trans. Magn.*, vol. 28, no. 2, pp. 1299-1302, Mar. 1992.

[25] B. Bolund, M. Leijon and U. Lundin, "Poynting Theorem Applied to Cable Wound Generators," *IEEE Trans. Dielectr. Electr. Insul.*, vol. 15, no. 2, pp. 600-605, Apr. 2008.

[26] D. Barth, B. Klaus and T. Leibfried, "Litz wire design for wireless power transfer in electric vehicles," *Proc. WPTC*, Taipei, May 2017.

[27] S. Wang, M. A. de Rooij, W. G. Odendaal, J. D. van Wyk and D. Boroyevich, "Reduction of high-frequency conduction losses using a planar litz structure," *IEEE Trans. Power Electron.*, vol. 20, no. 2, pp. 261-267, Mar. 2005.

[28] X. Tang and C. R. Sullivan, "Optimization of stranded-wire windings and comparison with litz wire on the basis of cost and loss," *Proc. PESC*, Aachen, Germany, vol.2, pp. 854-860, June 2004.